Supporting Information

Revealing Fundamentals of Charge Extraction in Photovoltaic Devices Through Potentiostatic Photoluminescence Imaging

Lukas Wagner[1,2,*], Patrick Schygulla[1,2], Jan Philipp Herterich[1,3], Mohamed Elshamy[1], Dmitry Bogachuk[1,2], Salma Zouhair[1,4], Simone Mastroianni[1,3], Uli Würfel[1,3], Yuhang Liu[5,*], Shaik M. Zakeeruddin[5], Michael Grätzel[5], Andreas Hinsch[1,*], Stefan W. Glunz[1,2]

[1] Fraunhofer Institute for Solar Energy Systems ISE, Heidenhofstraße 2, 79110 Freiburg, Germany.
Email: lukas.wagner@ise.fraunhofer.de, andreas.hinsch@ise.fraunhofer.de

[2] Laboratory for Photovoltaic Energy Conversion, University of Freiburg, Emmy-Noether-Straße 2, 79110 Freiburg, Germany.

[3] Freiburg Materials Research Center FMF, University of Freiburg, Stefan-Meier-Straße 21, 79104 Freiburg, Germany.

[4] Abdelmalek Essaadi University, FSTT, Thin Films & Nanomaterials Lab, 90000 Tangier, Morocco.

[5] Laboratory of Photonics and Interfaces (LPI), Department of Chemistry and Chemical Engineering, École Polytechnique Fédérale de Lausanne, Lausanne CH-1015, Switzerland.
E-mail: yuhang.liu@epfl.ch

Contents

A. Discussion of established imaging and mapping techniques

In solar cell research, mainly two approaches are followed for spatial resolved characterization of the active cell area, namely scanning-based “mapping” and camera-based “imaging” techniques. A range of approaches to determine the local photocurrent have been established for wafer-based solar cells such as GaAs or silicon photovoltaics (PV) and were also applied to emerging technologies like perovskite solar cells (PSC), namely light beam-induced local current (LBIC) mapping, lock-in thermography (LIT) imaging, as well as photoluminescence (PL) and electroluminescence (EL) based imaging techniques.[1,2] The opportunities and constraints of these characterization methods are briefly outlined in the following. An overview is presented in Table S1.

LBIC

The LBIC method allows recording photocurrent maps by locally illuminating the sample with a confined laser spot and measuring the induced local short-circuit photocurrent (J_{sc}) with high spatial resolution.[3–5] The acquisition time for one map at short circuit lies in the range of 30 minutes.

LIT

In dark lock-in thermography (DLIT) imaging, the local power dissipation of a non-illuminated sample is assessed by measuring the joule heating induced by an applied AC voltage via a lock-in infrared detector. The to assess the local $J(V)$ and local J_{sc}, several methods to fit equivalent circuit models to data acquired at different bias voltages have been proposed. [6,7] The weakness of all methods based on fitting data to an equivalent circuit model lies in the fact that, a range of datapoints are necessary for a good fit and, most importantly, the choice of the diode model has to be made *ex ante* and has a strong impact on the retrieved parameters.

Notably, for illuminated lock-in thermography (ILIT), an approach for Si-PV was developed based that allows assessing the local J_{sc} without fitting to a diode model.[8] Yet, the approach is based on the assumption that the photocurrent at reverse bias does not differ significantly from the J_{sc}. For PSC, reverse bias can induce device degradation,[9,10] which might explain why, to the best of our knowledge, this ILIT approach was so far not reported for PSC. Both LIT methods have the drawback that the low signal-to-noise ration requires long data acquisition times per images in the range of 20 to 60 minutes. [3] Especially for coupled electric-ionic semiconductors like perovskites, this approach may lead to measurement artefacts due to sample degradation or transient ionic effects due to the AC bias voltage.

Photoluminescence imaging

Employing PL images, based on various equivalent circuit models, a range of refined approaches for the spatial determination of the dark saturation current and series resistance[11–16] as well as local short circuit current[17] have been proposed for Si-PV. For perovskite solar cells, PL imaging so far has mainly been applied to study layer uniformity, crystallinity and degradation in perovskite solar cells under open circuit (PL(V_{oc})).[3,18–23] Recently, PL based series resistance imaging methods have also been applied to PSC.[24,25]

Electroluminescence imaging

Electroluminescence imaging is based on the principle of inducing luminescence by injection of charge carriers via the application of a forward bias that is applied to the device in the dark. For photocurrent imaging, EL has, however, only the potential to assess the dark spatial $J(V)$ curves. Moreover, for perovskite PV meager signal-to-noise ratios are achieved even at forward bias above V_{oc} and for acquisition times of several minutes. For PSC, this does not only limit the spatial resolution but can also falsify the result due to an integration over transient effects.[22]

Table S1. Comparison of established photocurrent imaging / mapping techniques and the PPI method.

	Data acquisition method	**Data acquisition time per bias voltage (approximate) [min]**	**Applicable bias voltages**	**Steady state (spatially illumination)**	**Steady state (bias voltage)**	**Local $J(V)$ acquisition**
LBIC	mapping	30	0 V	no	yes	no*
DLIT	imaging	20 – 60	various	dark	yes	diode model fitting
ILIT	imaging	20 – 60	0 V and < 0 V	yes	yes	no
PL	imaging	< 1	various	yes	yes	diode model fitting
EL	imaging	1 - 10	> V_{oc}	dark	yes	direct
PPI	imaging	< 1	various	yes	yes	direct

* For Si-PV, Carstensen et al. presented an approach to reconstruct the local photocurrent at different bias voltages from fitting diode-models to LBIC data, however not at microscopic resolution.[26]

B. Theoretical relationship between the radiative and non-radiative recombination

Ideality factor of recombination currents

If the studied sample can be described by the Shockley diode equation, we can express the recombination current density $J_{\text{rec,i}}$ of a specific recombination mechanism (i) by [27,28]

$$J_{rec,i}(V) = J_{rec,i,0}\left[e^{\frac{\Delta E_f}{n_{id,i}k_B T}} - 1\right], \tag{S1}$$

where $J_{\text{rec,i,0}}$ is a material specific parameter, ΔE_{f} is the quasi fermi-level splitting (QFLS), k_{B} is the Boltzmann constant and T is the temperature. $n_{\text{id,i}}$ is the ideality factor of the specific recombination mechanism.

If the voltage drop across the contact layers is negligible, we can approximate the QFLS by the voltage at the outer terminals $\Delta E_f = eV$. Deviations of this case are discussed in Section C.

For $\Delta E_f = eV$, we can simplify two cases: close to the short circuit case ($V \rightarrow 0\text{V}$)

$$J_{rec,i}(\text{V}) \rightarrow 0. \tag{S2a}$$

This means that in the ideal case, all charge carriers are extracted outside of the cell in short circuit.

If the applied voltage is larger than the thermal voltage ($V_{\text{T}} = k_B T/e \approx 25.8\text{ mV} \ll V$), which is the case except for voltages close to short circuit, the equation can be approximated by

$$J_{rec,i}(V) = J_{rec,i,0}\, e^{\frac{V}{n_{id,i}V_{\text{T}}}}, \tag{S2b}$$

on which we focus in the following consideration.

The ideality factor can be expressed by[29]

$$n_{id} = \frac{m}{\delta}. \tag{S3}$$

Herein, m is a measure for the number of the charge carrier types (n or p for negative or positive charge carriers, respectively) that are involved in splitting the quasi Fermi levels: $np = n^m$ (or p^m). Herein $n = \Delta n + n_0$ and $p = \Delta p + p_0$, where $\Delta n,p$ being the (symmetrically) photoexcited charge carriers with $\Delta n = \Delta p$. n_0 is the background doping concentration. We can see that if the material is sufficiently doped ($n_0 >> \Delta n$, $p_0 << \Delta p$) then $n >> p$ (or vice versa) and hence m approaches one.

If the photogenerated charge carriers greatly excess the background doping concentration ($\Delta n = \Delta p >> p_0$, n_0, also known as high injection), then $n \approx p$ and $m \rightarrow 2$. This is most probably the case for typical perovskite photoabsorbers which, in contrast to Si-PV, have been reported to behave like intrinsic or low-doped semiconductors. [30–33]

The ideality factor is also influenced by the recombination reaction order δ. In open-circuit conditions, the reaction order describes how the effect of the charge carrier density n on the specific recombination

$$R_i = k_i n^{\delta}, \tag{S4}$$

with k_i being the recombination specific rate constant. Hence, δ can be imagined as the number of charge carriers that are involved in a recombination process (at the time when the process happens).

For the $n \approx p$, $m \rightarrow 2$ case, there are two recombination processes with clearly defined recombination orders: radiative and Auger recombination (the remaining Shockley-Read-Hall (SRH) recombination is discussed further below). For radiative or band-to-band recombination, two charge carriers are involved as a free electron recombines with a free hole, thereby emitting a photon. We can write

$$R_{rad} = k_{rad} np, \tag{S5}$$

and hence $\delta = 2$. For the recombination current this means that $n_{\mathrm{id,rad}} = 1$ and

$$J_{rad}(V) = J_{rad,0} e^{\frac{V}{V_{\mathrm{T}}}}. \tag{S6}$$

For Auger recombination, the recombination of an electron and a hole leads to the excitation of a third charge carrier, hence $\delta = 3$ and $n_{\mathrm{id,Auger}} = 2/3$. In contrast to Si-PV, PSC display low Auger recombination rate constants k_3,[33] which means that under normal illumination intensities around 1 sun, the contribution of Auger recombination to non-radiative recombination processes can be neglected.

The remaining contribution to non-radiative (SRH) recombination for PSC is still under debate and a range of different recombination processes with different specific ideality factors have been reported.[28,34] According to the considerations above $n_{\mathrm{id,n.r.}}$ needs to lie between 1 and 2. If the ideality factor if the entire *I-V* curve close to one then it is reasonable to assume that $J_{\mathrm{n.r.}}$ is either negligible or that $n_{\mathrm{id,n.r.}} \approx 1$. In this case, $J_{\mathrm{n.r.}}$ is linearly proportional to J_{rad} as expressed by $k = \mathrm{const.}$ in Equation (2).

Generalized form of Equation (5)

In the following, we consider the general case where

$$J_{n.r.}(V) = J_{n.r.,0} e^{\frac{V}{n_{id,nr} V_{\mathrm{T}}}}. \tag{S7}$$

Now, Equation (2) can be written as

$$J_{n.r.}(V) = k' \cdot J_{rad}(V)^{\frac{1}{n_{id,nr}}}, \tag{S8}$$

with $k' = \mathrm{const.}$

Then, Equation (1) yields

$$J(V) = J_{gen} - J_{rad}(V) - J_{n.r.}(V) = J_{gen} - J_{rad}(V) - k' \cdot J_{rad}(V)^{\frac{1}{n_{id,nr}}} \tag{S9}$$

Hence, if the relationship between J_{rad} and $J_{\mathrm{n.r.}}$ is unknown, then

$$\begin{aligned} S_{PL}(V_{oc}) - S_{PL}(V) &= \frac{c}{e}[J_{rad}(V_{oc}) - J_{rad}(V)] \\ &= \frac{c}{e}\left[J_{gen} - J_{n.r.}(V_{oc}) - J_{gen} + J(V) + J_{n.r.}(V)\right] \\ &= \frac{c}{e}\left[J(V) - \Delta J_{n.r.}(V)\right], \end{aligned} \tag{S10}$$

with $\Delta J_{\mathrm{n.r.}}(V) = J_{\mathrm{n.r.}}(V_{\mathrm{oc}}) - J_{\mathrm{n.r.}}(V)$.

The normalized difference between the PL signal at two voltages can now be expressed in the general form of

$$\frac{S_{PL}(V_{oc}) - S_{PL}(V)}{S_{PL}(V_{oc})} = \frac{J(V) - \Delta J_{n.r.}(V)}{J_{gen} - J_{n.r.}(V_{oc})} =: c_{ex}(V). \tag{S11}$$

In conclusion, for the case of $n_{\mathrm{id,n.r.}} \neq 1$ the approach does not yield an exact assessment of the local photocurrent since the local non-radiative recombination currents at V_{oc} are unknown. Yet, the approach can be still employed as a figure of merit for local charge extraction, as expressed by a charge extraction coefficient $c_{\mathrm{ex}}(V)$.

Finally, we point out that by comparing the $c_{\mathrm{ex}}(V)$ image with a complementary photocurrent imaging/mapping method the approach can be used to qualitatively assess the spatially resolved non-radiative ideality factor or internal voltage loss which gives instructive insights in the internal loss mechanisms that induce recombination and hamper charge extraction.

C. Accounting for internal voltage and current losses

The condition $\Delta E_f = eV$ in Equation S1 may not be fulfilled die to an internal voltage loss. This can occur inside the photoactive layer if there is a diffusion limited current which creates an implied voltage inside the device.[15] The voltage can also be lost across contact layers due to due to contact resistance at the interfaces with CELs or due to resistance of the CEL itself.[35] Finally, photogenerated charge carriers may be lost due to shunt resistance, e.g., via pinholes that allow electrical contact between the CELs. In a first order approximation, such processes can be accounted for if we consider local series and shunt resistances, R_{s} and R_{sh}, respectively. Now, we can distinguish between the current densities and voltage measured at the outer solar cell cables, $J(V)$ and V, respectively, and the internal current density and voltage, $J_{\mathrm{int}}(V_{\mathrm{int}})$ and V_{int}, respectively, as depicted in Figure S1. For the sake of readability, in the following ‚R‘ represents the resistances divided by the considered area.

Figure S1 shows that

$$J(V) = J_{int}(V_{int}) - \frac{V_{int}}{R_{sh}} = J_{int}(V_{int}) - \frac{J(V) \cdot R_s + V}{R_{sh}}. \tag{S12}$$

If the solar cell follows the Shockley equation, as discussed above we can write

$$J_{int}(V_{int}) = J_{gen} - J_{rad,0}\left[e^{\frac{V + J(V)\cdot R_s}{n_{id,rad}V_{\mathrm{T}}}} - 1\right] - J_{n.r.,0}\left[e^{\frac{V + J(V)\cdot R_s}{n_{id,nr}V_{\mathrm{T}}}} - 1\right]. \tag{S13}$$

This yields

$$J(V) = J_{gen} - J_{rad,0}\left[e^{\frac{V+J(V)\cdot R_s}{n_{id,rad}V_{\mathrm{T}}}} - 1\right] - J_{n.r.,0}\left[e^{\frac{V+J(V)\cdot R_s}{n_{id,nr}V_{\mathrm{T}}}} - 1\right] - \frac{V + J(V)\cdot R_s}{R_{sh}}. \tag{S14}$$

For Equation S11, this implies

$$\frac{S_{PL}(V_{oc}) - S_{PL}(V)}{S_{PL}(V_{oc})} = \frac{J_{rad,0}\left[e^{\frac{V_{oc}+J(V_{oc})\cdot R_s}{n_{id,rad}V_{\mathrm{T}}}} - 1\right] - J_{rad,0}\left[e^{\frac{V+J(V)\cdot R_s}{n_{id,rad}V_{\mathrm{T}}}} - 1\right]}{J_{rad,0}\left[e^{\frac{V_{oc}+J(V_{oc})\cdot R_s}{n_{id,rad}V_{\mathrm{T}}}} - 1\right]} \tag{S15a}$$

or

$$\frac{S_{PL}(V_{oc}) - S_{PL}(V)}{S_{PL}(V_{oc})} = \frac{J(V) - \frac{V + J(V)\cdot R_s}{R_{sh}} - \Delta J_{n.r.}(V + J(V)\cdot R_s)}{J_{gen} - J_{n.r.}(V_{oc} + J(V)\cdot R_s)}. \tag{S15b}$$

In other words, the working point of the radiative recombination current, i.e., the PL signal, is influenced by the series resistance. Moreover, the shunt resistance induces an additional recombination path for the (internal) photocurrent.

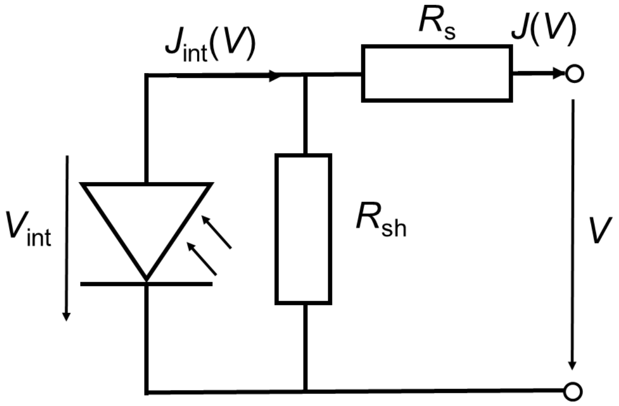

Figure S1. Equivalent circuit of a solar cell spot with shunt and series resistances, R_s and R_{sh}, respectively.

D. Epitaxial Growth and Characterization of a III-V solar cell

The GaInAsP solar cell was grown using metalorganic vapor phase epitaxy on a commercial AIXTRON AIX2800G4-TM reactor. Trimethylgallium and trimethylindium were used as precursors for the group-III elements, and arsine and phosphine for the group-V elements. Silane was used for n-type and dimethylzinc for p-type doping. Standard growth temperatures and V/III ratios were used. The cell structure is depicted in Figure S2. It consists of a thick n-type $Ga_{0.91}In_{0.09}As_{0.83}P_{0.17}$ absorber above a heterojunction interface to a higher band gap $Al_{0.3}Ga_{0.7}As$ layer. This rear-heterojunction cell architecture allows exploiting the higher carrier lifetimes in n-type $Ga_{0.91}In_{0.09}As_{0.83}P_{0.17}$ and reducing recombination in the space charge region.[36] More details on the growth process are reported elsewhere [37].

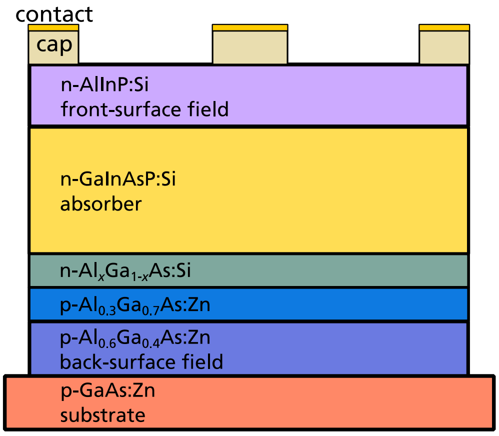

Figure S2. Schematic solar cell layer structure of the epitaxially grown GaInAsP solar cell.

From the epitaxial layer structure two types of solar cells were processed on the same wafer: larger devices with a mesa area of 4 cm² and smaller devices with a mesa area of 0.06 cm². The current-voltage characteristics of one of the large solar cells was measured under calibrated conditions with an AM1.5g solar spectrum in the Calibration Laboratory of Fraunhofer ISE (CalLab). The $I(V)$-curve was modelled using a one-diode equation [38]:

$$J(V) = J_0\left(\exp\left(\frac{qV - R_s\,J(V)}{nkT}\right) - 1\right) + \frac{qV - R_s\,J(V)}{R_\mathrm{p}} - J_\mathrm{ph}. \qquad \text{(S16)}$$

The measured and modelled curve are both shown in Figure S3. The cell exhibits a diode ideality factor of 1.04, a dark recombination current of 8.23×10^{-21} mA/cm², a very high shunt resistance of 9.19 kΩ cm², and a very low series resistance of 0.603 Ω cm². In order to confirm the low series resistance a suns-V_{oc} measurement was conducted on a WCT-120 Sinton Instruments device.[39] Thanks to its currentless measuring mode this method allows to obtain a relative $I(V)$-curve without series resistance effects that can be scaled to the short-circuit current. In Figure S3 the standard $I(V)$-curve is compared to the suns-V_{oc} IV-curve. Both curves coincide to a high degree. Around the open-circuit point the suns-V_{oc}-curve is even 10 meV below the calibrated curve which is likely due to the slightly different spectrum used for the suns-V_{oc}-measurement.

The PPI measurements, which employ an excitation spot much smaller than the area of the large cell, were performed on the small device in order to achieve an excess carrier density similar to AM1.5g. For the reported PPI and PL data, detector counts of a device region without metallization grid was selected. The external quantum efficiency (EQE) was measured on a large cell. Its absolute height was normalized so that the integrated photocurrent matches the short-circuit current density of the calibrated AM1.5g $I(V)$-curve (correction factor 1.07). The internal quantum efficiency $IQE =$

$EQE/(1-R)$ was then calculated from the EQE by including the reflectance R(620 nm) = 0.286 (cf. Figure S4). The procedure to measure EQE and PPI on two different cells was necessary because of the difficulty of an accurate EQE measurement on a small solar cell. Considering the effects of shadowing due to a different metal grid on these two devices (correction factor 1.03), and given the fact that both cells have exactly the same epitaxial structure as they were processed on the same wafer, the EQE and PPI results can still be compared with each other. However, the resulting uncertainty of this comparison is expected to be high because of the high number of measuring techniques (EQE, reflectance, short-circuit current, PPI) involved that each add a little uncertainty to the calculation.

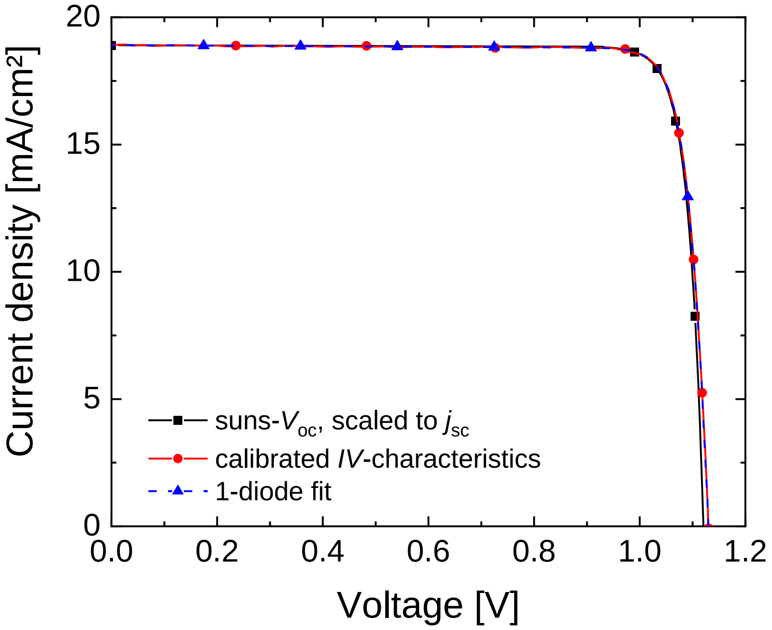

Figure S3. Comparison of a calibrated current-voltage characteristics under AM1.5g (red), suns-V_{oc} characteristics scaled to the calibrated results (black), and a 1-diode model fit to the calibrated data (blue, dashed). The agreement between the curves shows the low series resistance, the high parallel resistance, and the ideality factor close to unity.

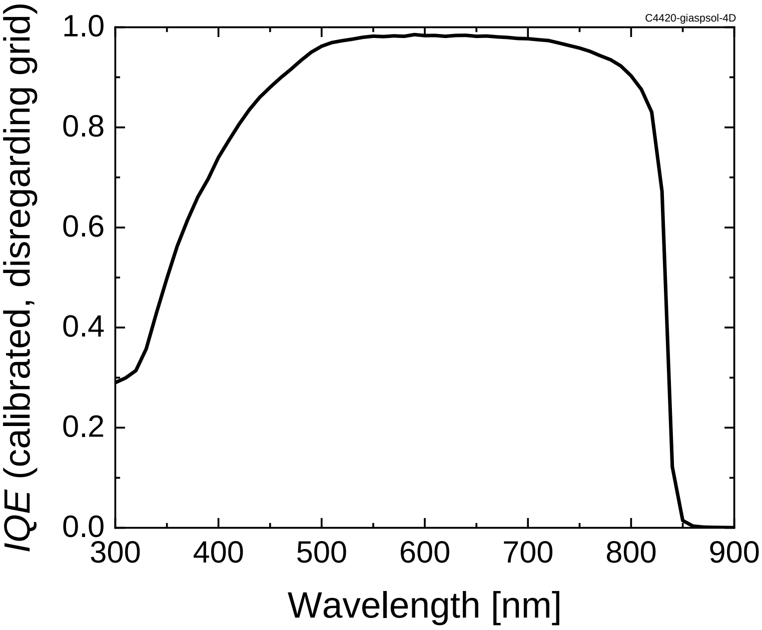

Figure S4. Internal quantum efficiency (*IQE*) of the 4 cm² GaInAsP solar cell as a function of wavelength. The curve was normalized to the calibrated AM1.5g short-circuit current density. The amount of grid shadowing was determined and corrected for so that a comparison to the PPI results, evaluated in a region of interest without metal grid, from the small solar cell becomes possible.

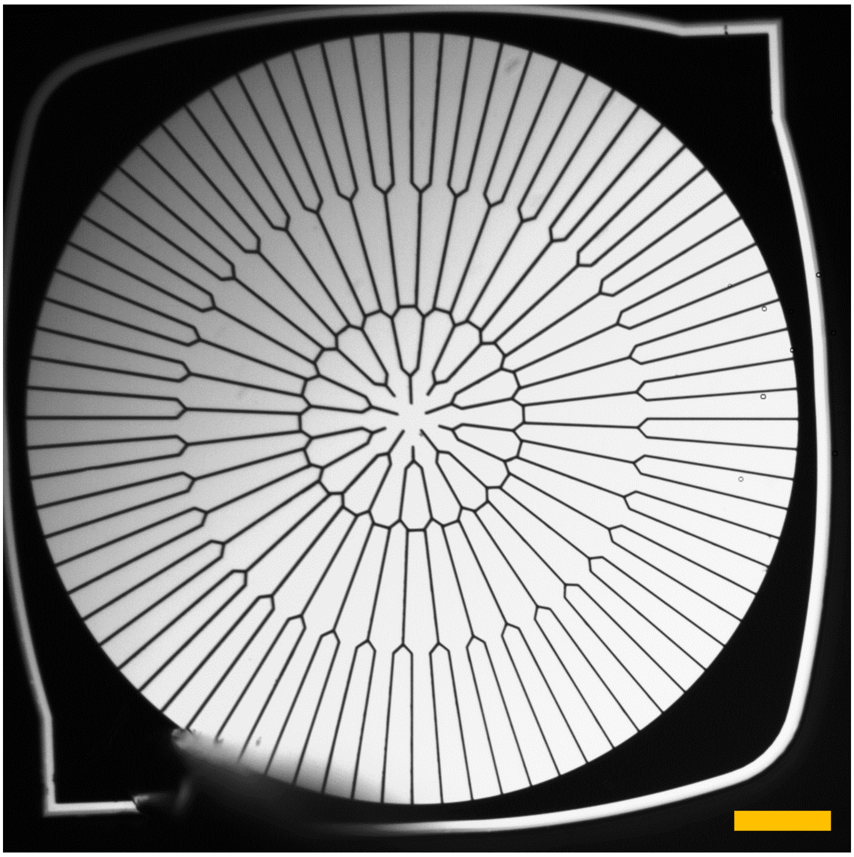

Figure S5. Photoluminescence microscopy image of the tested small GaInAsP cell in open circuit. The circular active area is covered with a front metallization grid. The yellow scale bar represents 300 µm.

E. Perovskite solar cells fabrication

Materials: Lead iodide and cesium iodide are purchased from TCI co, ltd. Formamidinium iodide, methyl ammonium iodide and $N^2,N^2,N^{2'},N^{2'},N^7,N^7,N^{7'},N^{7'}$-octakis(4-methoxyphenyl)-9,9′-spirobi[9*H*-fluorene]-2,2′,7,7′-tetramine (Spiro-OMeTAD) are purchased from Dyesol. Ultra-dry dimethylformamide (DMF), ultra-dry dimethyl sulfoxide (DMSO) and ultra-dry chlorobenzene (CB) is purchased from Acros, dry isopropanol (IPA), 4-*tert*-butyl pyridine, lithium bistrifluorosulfonyl imide (LiTFSI), acetyl acetone, titanium diisopropoxide bis(acetylacetonate), 75 wt. % in isopropanol and borane tetrahydrofuran complex solution (1.0 M in THF) are purchased from Sigma-Aldrich. All the chemicals are used as received without further purification. Conductive glass, Fluorine-doped tin oxide (10 Ω/sq) is purchased from Nippon Sheet Glass, Titanium dioxide paste (30 NRD) is purchased from Dyesol.

Substrate preparation: Nippon Sheet Glass (NSG, 10 Ω/*sq*) was consecutively cleaned using 2% Hellmanex aqueous solution, deionized water, acetone and ethanol by sonicating for 20 min for each solvent. After drying with compressed air, UV-Ozone was applied for further cleaning. Compact TiO_2 is deposited on top of FTO using spray pyrolysis method: the substrates are preheated to 450 °C; a precursor solution of titanium diisopropoxide bis(acetylacetonate), 75 wt. % in isopropanol is diluted with dry ethanol with a volume ratio of 1:9 and addition 4% volume ratio of additional acetyl acetone. After spray pyrolysis, the FTO/TiO_2 substrate is allowed to heat at 450 °C for 30 min before cooling down to room temperature. Mesoscopic TiO_2 is applied by spincoating a diluted solution of 30 NR-D paste (mass ratio of paste:EtOH = 1:6) at 4000 rpm with acceleration of 2000 rpm/s. The as-prepared FTO/compact-TiO_2(c-TiO_2)/TiO_2 paste was then allowed to sinter at 450 °C for 1 h, yielding FTO/c-TiO_2/mesoscopic-TiO_2, which is then deposited with perovskite freshly.

Perovskite deposition: Pure 3D perovskite precursor solution is prepared by dissolving a mixture of lead iodide (736.5 mg, 1.60 mmol), formamidinium iodide (237.3 mg, 1.38 mmol), methylammonium iodide (9.5 mg, 0.06 mmol) and cesium iodide (15.6 mg, 0.06 mmol) in 1 mL mixed solution of DMF and DMSO (DMF (*v*):DMSO (*v*) = 4:1) under mild heating condition at ~70 °C to assist dissolving. The perovskite active layer is deposited using anti-solvent method, with chlorobenzene as anti-solvent. The perovskite precursor solution is deposited on the freshly-prepared FTO/c-TiO_2/m-TiO_2 substrate, a two-step spincoating method is applied. 1st step is proceeded at 1000 rpm with acceleration rate of 200 rpm/s for 10s. 2nd step is followed by 5000 rpm with acceleration rate of 2000 rpm/s for 20 s. 200 µL of CB is applied at the 10th second. After spin coating, the substrate is allowed to anneal at 110 °C for 40 min. The whole procedure is done in a nitrogen-filled glovebox.

Hole-transporting layer and gold back contact: Spiro-OMeTAD is selected as hole-transporting layer (HTL) material. Spiro-OMeTAD is dissolved in chlorobenzene with a concentration of 70 mM, which is doped by LiTFSI and 4-*tert*-butyl pyridine, and the molar ratios are 33% and 330%, respectively. The mixed Spiro-OMeTAD solution was spin-casted on the surface of the perovskite at 4000 rpm for 30 s. The acceleration is 2000 rpm/s. The gold electrode is thermally evaporated on the surface of the HTL with the shadow mask with an area of 5 mm * 5 mm. The thickness of gold electrode is 80 nm, and the evaporation speed is adjusted to 0.01 nm/s at the first 10 nm, and 0.08 nm/s for the rest of the procedure.

Photovoltaic performance measurements: Stabilized *I-V* parameters were measured under a class A xenon arc lamp solar simulator with a Keithley 2400 source meter. The light intensity was calibrated with a calibrated silicon cell. For the measurement of the stabilized PCE, the photocurrent was measured while the device was biased at a constant voltage close to maximum power point.

F. Stabilized *I*-*V*-parameters of the high-efficient perovskite device

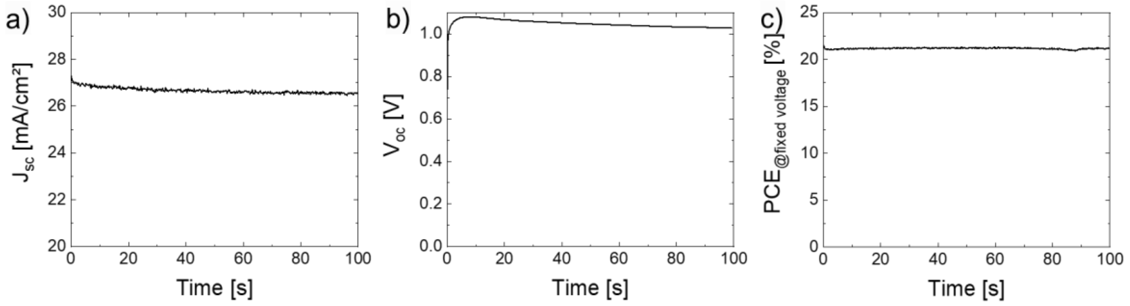

Figure S6. Stabilized J_{sc}, V_{oc}, and PCE (measured at a fixed voltage) of the high-efficient cell discussed in Figure 2. The device was measured under a class A solar simulator with a shadow mask of 0.09 cm².

G. $J_{sc}/J_{gen}|_{PL}$ measurement of perovskite devices at different wavelengths

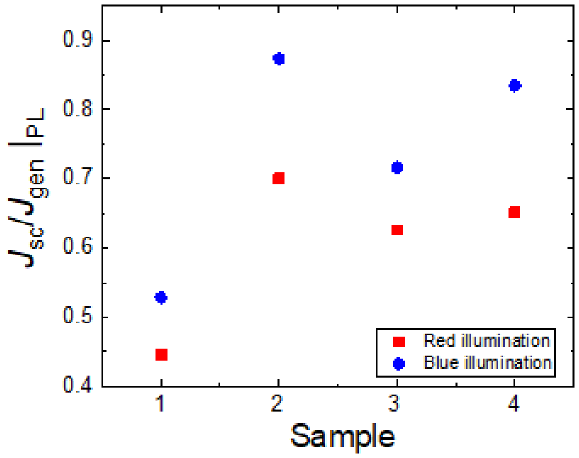

Figure S7. $J_{sc}/J_{gen}|_{PL}$ averaged over the entire microscope image for four different PSCs, probed under red (623 nm) and blue (405 nm) LED illumination.

H. Calibration and error sources for qualitative $J_{sc}/J_{gen}|_{PL}$ imaging

Uncertainty discussion

Although the principle is straightforward, it is important to note that the significance of the here presented method is restricted to a range of fundamental and technical limitations which have to be assessed carefully. First, photon-reabsorption is not considered. Second, we cannot regard lateral diffusion currents that lead to an equilibration of charge densities from the 'high-performing' spots (which are slightly underestimated) and to the 'poorly performing' spots (which are slightly overestimated). Third, due to the light source of the measurement system, the depths of excitation wavelength can be different from an AM1.5g illumination (measurements under different excitation wavelengths are presented in Figure S7). Fourth, defining the steady state of the perovskite solar cell can be challenging and may vary from one sample to the other, as further discussed below. Finally, a detailed discussion of the effect of the diode ideality factor as well as internal (resistive) voltage and current losses can be found in Section B and C.

Moreover, we note from own experience that it is crucial to ensure homogeneous illumination of the entire active cell area. For samples with highly conductive electrodes, as present in the tested III-V and perovskite devices, illumination with a light spot smaller than the active area leads to a lateral distribution of charge carriers via the electrodes when the probe is biased in in open circuit. This induces radiative recombination in the non-illuminated regions and hence reduces the measured PL signal in the illuminated region. As this effect is less pronounced for bias voltages closer to short circuit, this leads to an underestimation of $J_{\mathrm{sc}}/J_{\mathrm{gen|\ PL}}$.

Calibration based on reference solar cell

The precise quantitative determination of the $J(V)$-image from PL requires especially the determination of the PL signal intensity of the camera detector if a PL of zero is expected which is for example influenced by leakage of light through the optical filter and detector noise, as discussed in the results section. Ideally, the setup should therefore be calibrated using a reference device for which J_{sc}/J_{gen} is known.

In the following, the high performing (stabilized PCE = 21.2 %) perovskite cell (cf. Figure 2 and Figure S6) is employed to discuss the calibration of the setup. For the studied solar cell with a band-gap of 1.54 eV (805 nm) and an ideal EQE of 100 % between 300 nm to the band gap, the highest possible photocurrent under AM1.5g (ASTM G-173) is $J_{\mathrm{gen,max}} = 27.6$ mA/cm². The determined stabilized J_{sc} of J_{sc} of 26.4 mA/cm² (cf. Figure S6) amounts to 95.7 % of this theoretical limit. Assuming an ideal photo absorption (maximum $J_{\mathrm{gen}} = J_{\mathrm{gen,max}}$), the highest $J_{\mathrm{sc}}/J_{\mathrm{gen}}$ is 0.96. Therefore, the sample could be used to calibrate the measurement setup. However, this approach is not fully satisfying for two reasons: first, it does not help to correctly assess the baseline of the PL measurements. Second, as shown in Figure S8, the device does not yield a completely homogeneous pattern for $J_{\mathrm{sc}}/J_{\mathrm{gen|\ PL}}$ which would mean that some areas need to be assigned with unphysical values larger than one.

Calibration by baseline assessment

Hence, a base-line correction for the PL setup was implemented by means of an alternative reference sample. Such a sample should induce the same parasitic signals in the detector but without the PL of the tested sample.

For the measurements of the III-V device, the baseline calibration was carried out by measuring the reflectance of the sample at a wavelength close to the microscope excitation wavelength and a measurement of the PL signal of the highly reflective front electrode metallization of the sample.

For the perovskite devices, a stack of glass / TCO / m-TiO_2 / ZrO_2 / carbon-graphite was fabricated to resemble a PSC without perovskite. This serves as a baseline to account for reflections and scattering from the different layers, whereas that the reflection from the (black) carbon-graphite layer can be assumed to approach zero. As shown in Figure S11, for very thin perovskite absorber layers, back-reflection of PL light from the gold electrode can have a significant impact on the measurement whereas for typical device thicknesses, the effect of optical reflection is over-compensated by a higher charge-recombination due to the presence of a metal electrode.

A second challenge lies in the choice of the most suitable light source. Ideally, the device should be illuminated by the AM1.5g solar spectrum. However, this is not possible as this spectrum overlaps with the PL spectrum of the solar cell. We investigated two LED light sources with a wavelength below the PL wavelength of red (632 nm) and blue (405 nm) light. Here, a trade-off needs to be made: The red light resembles the absorption depth of the AM1.5g spectrum acceptably well whereas the blue light is absorbed by the first few 100 nm of perovskite.[40] PL images recorded under blue light will therefore overestimate effects associated with processes of charge-carrier absorption and recombination at the front electrode. For the red light, however, the parasitic effect of the excitation light reflected from the sample and entering the detector is higher as there is a non-negligible overlap between the transmittance of the filter on the detector and the spectrum of the red LED.

Figure S6 shows the comparison of the PL(V_{oc}) (a) and the $J_{sc}/J_{gen}|_{PL}$ image (b, c) under 632 nm and 405 nm LED illumination equivalent to the photon-flux of 1 sun, respectively. Notably, even after this baseline-correction, the $J_{sc}/J_{gen}|_{PL}$ averaged over the entire image for the two illumination sources was not identical. Under blue illumination it was estimated to 0.84 whereas for red illumination it was only 0.65.

Revealingly, the spots with the highest PL(V_{oc}) intensity typically are reflected in the $J_{sc}/J_{gen}|_{PL}$ image by a region with a high $J_{sc}/J_{gen}|_{PL}$ that has a very low value in the center (cf. feature i). However, there are also features where this low center spot is not present, such as in ii).

In conclusion, the above discussion underlines the importance of accurate calibration and stresses that the quantitative analysis of the $J_{sc}/J_{gen}|_{PL}$ image needs to be carried out with care. Still, for a fast qualitative assessment of spatially distributed inhomogeneities, even a non-optimal setup is well suited, and the base-line correction can serve to assess the lowest limit of the optically determined J_{sc}. In the following, where we focus on qualitative comparison, the red LED is employed, as it resembles better the absorption under solar illumination.

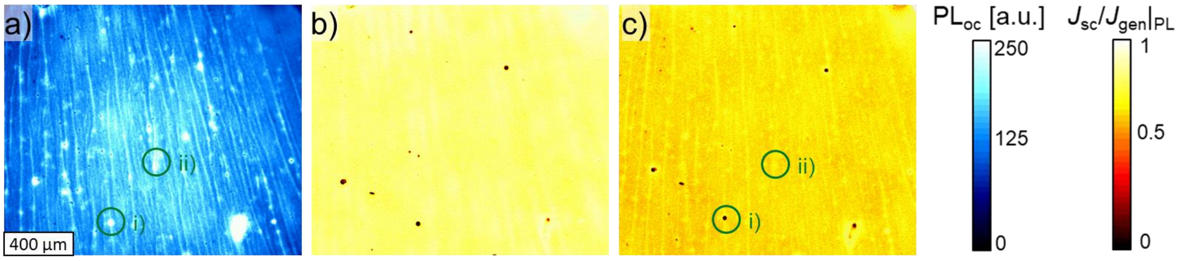

Figure S8. a) PL(V_{oc}) and (b, c) $J_{sc}/J_{gen}|_{PL}$ here determined from two PL images at open and short circuit of a high performing PSC. The device was illuminated with a blue (405 nm, b) and red LED (632 nm, c). Figure (a) and (c) are identical with Figure 2a and b and have been reprinted for comparison. The scale bar corresponds to 400 µm.

I. Further analysis of *PL*(*V*) and *I*(*V*) curves of the perovskite device

Figure S9 shows scaled representations of the local $J(V)/J_{gen}|$PL from Figure 3, normalized by the PL at short circuit. This representation can be used to compare the shape of the $J(V)/J_{gen}|_{PL}$ curves if the effect of different short circuit currents is ignored. Comparing Figure S9a with Figure 3c, it can be clearly seen that although the PL intensity of various spots reacts differently to the change of the bias voltage, $J(V)/J_{gen}|_{PL}$ follows the same exponential shape. This is can be further asserted by a semi-logarithmic representation, as shown in Figure S9b, displaying perfectly parallel and straight lines. The reason why the line is not continued for $V < 0.6$ V is probably due to a limited sensitivity of the PL camera at low changes of the PL intensity.

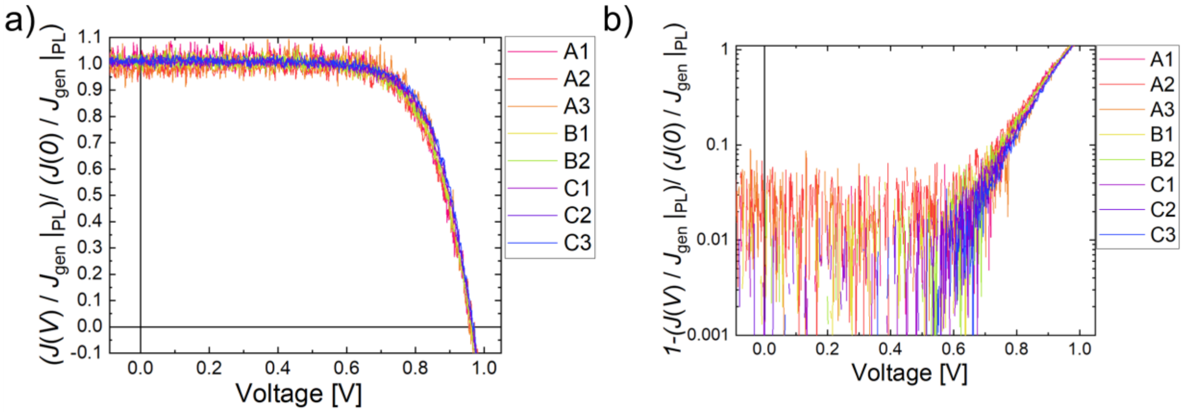

Figure S9. a) $J(V)/J_{gen}|_{PL}$ curves of the spots discussed in Figure 3, scaled by the respective local short circuit current $J(0)/J_{gen}|_{PL}$. b) Semi-logarithmic representation, whereby the values from a) were subtracted from one.

Figure S10a shows the average PL intensity (black curve) of the entire cell area measured during the voltage sweep displayed in Figure 3. For comparison, the current of the entire cell as measured in parallel is plotted (red). While the curves match up comparably well, it is interesting to note that the slope of the PL(V) curve is lower than that of the $I(V)$ curve. From the considerations outlined below, one would rather expect the opposite if the cell was affected by a series resistance or by a non-ideal the diode ideality factor ($n_{id} > 1$). It appears that either the effects are compensated for by an unknown third effect or the two effects do not to affect the studied device.

In Figure S10b, the curves are plotted in a semi-logarithmic plot to allow a better comparison of the exponential shape of the curves. For this representation, the curves were scaled as follows. The current was scaled to $I_{scaled}(V) = (1 - I(V)/I_{sc})$ and the PL was scaled to $PL_{scaled}(V) = (1-(PL(V_{oc})-PL(V))/PL(0))$.

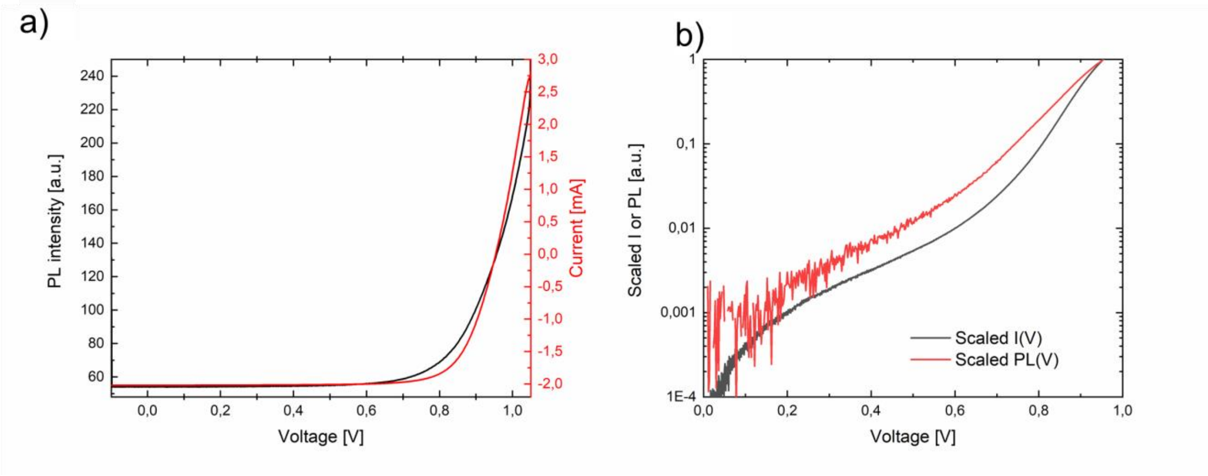

Figure S10. a) Average PL intensity of the entire observed cell area (left axis, black curve) and the photocurrent (right axis, red curve) that was measured during the voltage sweep displayed in Figure 3. b) Scaled, semi-logarithmic representation of these curves.

J. Influence of the gold electrode on the PL(V_{oc}) in perovskite devices

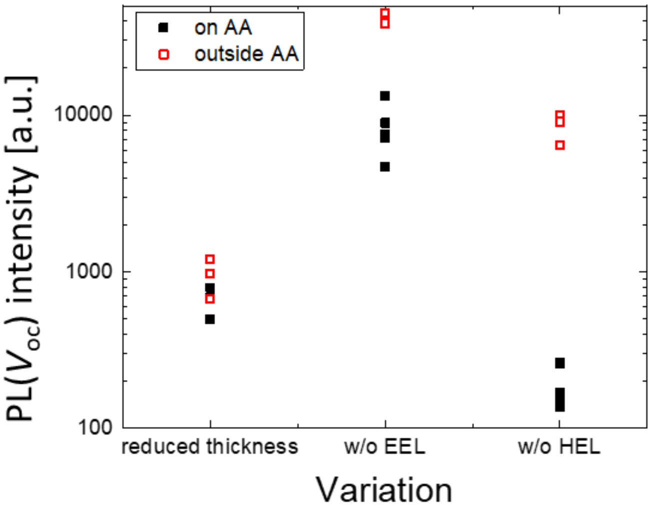

Figure S11. PL(V_{oc}) intensity for a PSC range of samples with reduced thickness, without EEL and without HEL. The plot compares the PL(V_{oc}) intensity measured on and outside the active area (AA), i.e., the region where the gold back electrode is deposited.

K. Stabilized *I-V* parameters of further perovskite devices

Figure S12a shows the stabilized V_{oc}, as measured under a solar simulator, with the stabilized PL(V_{oc}) measured under the PL microscope, for a range of samples with reduced thickness, without HEL or without EEL. The highest PL(V_{oc}) is achieved with EEL-free devices, which show however only moderate stabilized V_{oc}. Hence, the trend of the PL(V_{oc}) does not represent to observed V_{oc}. In contrast, the $J_{sc}/J_{gen}|_{PL}$ representation reflects much better the stabilized V_{oc} as shown Figure S12b. This demonstrates once more that the PL(V_{oc}) alone it is suited to estimate the device performance.

In Figure S12c, the stabilized J_{sc} estimated from the solar simulator are compared with the $J_{sc}/J_{gen}|_{PL}$ estimated from the PL microscope. The dashed line represents the ideal case where $J_{gen} = J_{gen,max} = 27.6$ mA/cm². The measured values are overall in agreement with the expected, linear relation. Especially the values of the samples with reduced thickness lie below close to the dashed line (except for one outlier). The values of the devices without EEL and HEL lie above the dashed line. This could mean that J_{gen} is below $J_{gen,max}$ due to non-ideal absorption or photogeneration. Especially for the HEL-free devices with very low photocurrents and PL intensities, the deviation could be due to the limitation of the method as discussed in the manuscript such as a non-ideal calibrated PL baseline.

Although we did not focus on the dependence of V_{oc} and FF on the PL in this work, it is yet interesting to consider the show seemingly linear relationship between the stabilized PCE and $J_{sc}/J_{gen}|_{PL}$ as shown in Figure S12d.

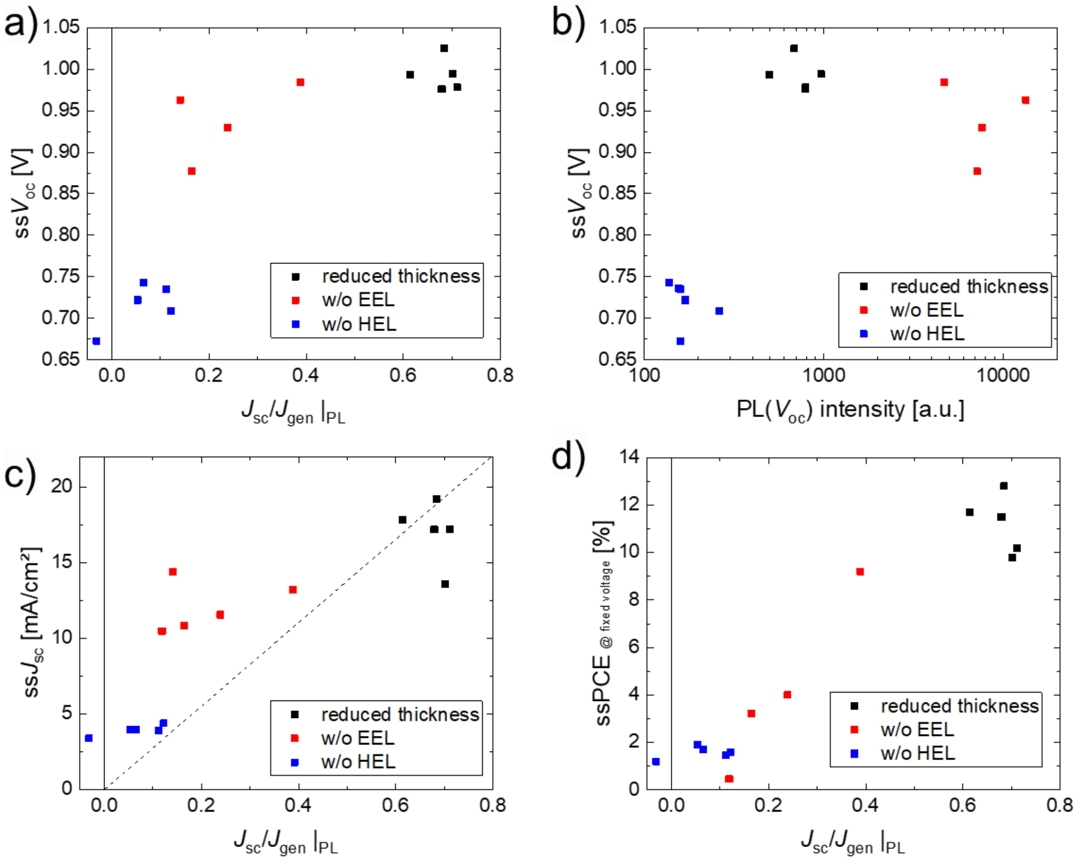

Figure S12. Stabilized V_{oc}, J_{sc} and PCE (measured under at a fixed voltage close to mpp) as obtained from measurements at a class A solar simulator for a range of devices with a reduced perovskite thickness (red), without EEL (blue) or without HEL (magenta). The values are plotted against PL(V_{oc}) or J_{sc}/J_{gen} |PL, as obtained from a measurement at a PL microscope under red (623 nm) LED illumination.

L. Spatial analysis of transient behaviour in perovskite devices

A further look at the local, transient effects of the spots in Figure 3 is presented in Figure S13. It shows the progression of the PL(V) intensity of these spots for different applied electrical bias, consecutively switching from V_{oc} to maximum power point (V_{mpp}) again to V_{oc}, to short circuit (0 V), and again to V_{oc}, respectively with a dwell time of 60 seconds each. V_{mpp} refers to the voltage at maximum power point as determined by a previous J-V sweep from V_{oc} to 0 V.

Regarding the spots in groups A, B, and C, despite the difference in PL intensity, the transient reaction to a switch of the voltage bias is very similar. Again, the last switching is the most significant with a high overshoot of the PL intensity upon switching to open circuit, followed by rapid decrease within few seconds and a slower convergence to a steady-state value. It is instructive to compare the three different steps of V_{oc}: one initial step ($0 < t < 60$ s) before which the device has already been illuminated at open circuit for longer than five minutes. A second step ($120 < t < 180$ s) before which the cell was biased at V_{mpp}. Moreover, a third step ($t > 240$ s) that was preceded by a working point at short circuit. The effect of switching from V_{mpp} to V_{oc} is marginal and the initial steady-state value from the first step is reached to the greatest extent within few seconds. In contrast, there is a strong overshoot of PL when switching from short circuit to V_{oc} in the third step. Here, the PL intensity does only stabilize and recover to the initial value for spots of group B while the PL is still decreasing after 60 s for spots of group C. The PL of spots of the group A increases during the process of switching – reaching PL intensities of group B in the final step - although it appeared to be stable in the first step at V_{oc}. Note that all spots exhibit a stabilized low PL upon switching to short circuit ($180 < t < 240$ s).

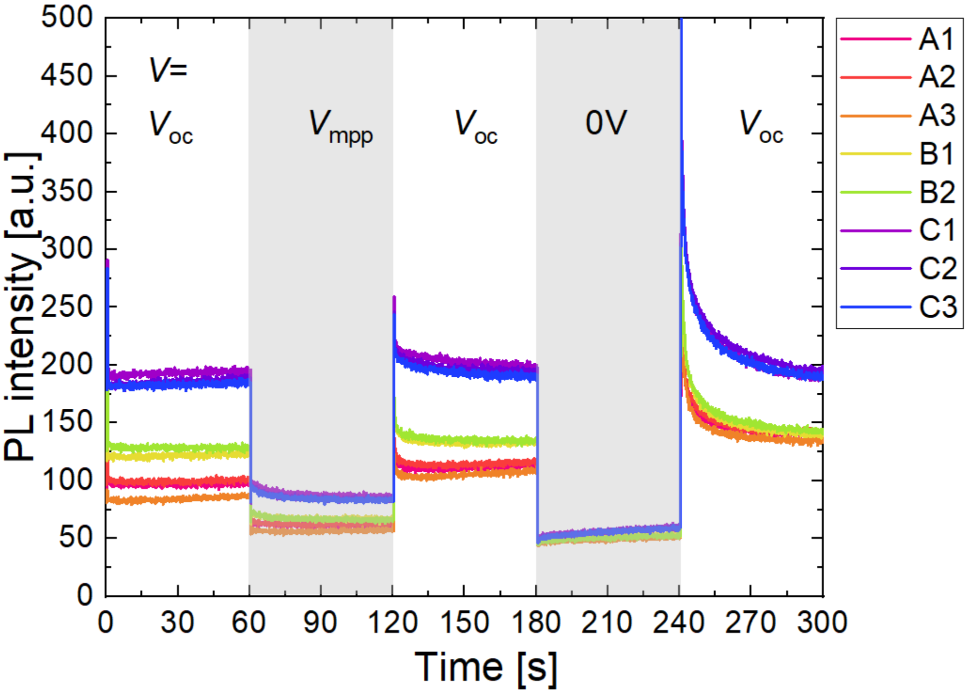

Figure S13. Transient evolution of the PL intensity at each spot of the sample depicted in Figure 3 for a successive bias of V_{oc}, V_{mpp}, V_{oc}, 0 V, and V_{oc} for 60 seconds each.

References

1. Schubert, M. C., Mundt, L. E., Walter, D., Fell, A. & Glunz, S. W. Spatially Resolved Performance Analysis for Perovskite Solar Cells. *Adv. Energy Mater.,* 1904001; 10.1002/aenm.201904001 (2020).
2. Fertig, F. *et al.* Short-circuit Current Density Imaging Methods for Silicon Solar Cells. *Energy Procedia* **77,** 43–56; 10.1016/j.egypro.2015.07.008 (2015).
3. Mundt, L. E. *et al.* Quantitative Local Loss Analysis of Blade-Coated Perovskite Solar Cells. *IEEE Journal of Photovoltaics*, 1–8; 10.1109/JPHOTOV.2018.2888835 (2019).
4. Seager, C. H. The determination of grain-boundary recombination rates by scanned spot excitation methods. *J Appl Phys* **53,** 5968–5971; 10.1063/1.331389 (1982).
5. Padilla, M., Michl, B., Thaidigsmann, B., Warta, W. & Schubert, M. C. Short-circuit current density mapping for solar cells. *Solar Energy Materials and Solar Cells* **120,** 282–288; 10.1016/j.solmat.2013.09.019 (2014).
6. Breitenstein, O. Nondestructive local analysis of current–voltage characteristics of solar cells by lock-in thermography. *Solar Energy Materials & Solar Cells* **95,** 2933–2936; 10.1016/j.solmat.2011.05.049 (2011).
7. Breitenstein, O., Fertig, F. & Bauer, J. An empirical method for imaging the short circuit current density in silicon solar cells based on dark lock-in thermography. *Photovoltaics, Solar Energy Materials, and Technologies: Cancun 2010* **143,** 406–410; 10.1016/j.solmat.2015.07.027 (2015).
8. Fertig, F., Greulich, J. & Rein, S. Spatially resolved determination of the short-circuit current density of silicon solar cells via lock-in thermography. *Appl Phys Lett* **104,** 201111; 10.1063/1.4876926 (2014).

9. Razera, R. A. Z. *et al.* Instability of p–i–n perovskite solar cells under reverse bias. *Journal of Materials Chemistry A* **8,** 242–250; 10.1039/C9TA12032G (2020).

10. Bowring, A. R., Bertoluzzi, L., O'Regan, B. C. & McGehee, M. D. Reverse Bias Behavior of Halide Perovskite Solar Cells. *Adv. Energy Mater.* **8,** 1702365; 10.1002/aenm.201702365 (2018).

11. Trupke, T., Pink, E., Bardos, R. A. & Abbott, M. D. Spatially resolved series resistance of silicon solar cells obtained from luminescence imaging. *Appl Phys Lett* **90,** 93506; 10.1063/1.2709630 (2007).

12. Kampwerth, H., Trupke, T., Weber, J. W. & Augarten, Y. Advanced luminescence based effective series resistance imaging of silicon solar cells. *Applied Physics Letters* **93,** 202102; 10.1063/1.2982588 (2008).

13. Glatthaar, M. *et al.* Evaluating luminescence based voltage images of silicon solar cells. *J Appl Phys* **108,** 14501; 10.1063/1.3443438 (2010).

14. Glatthaar, M. *et al.* Spatially resolved determination of dark saturation current and series resistance of silicon solar cells. *physica status solidi (RRL) - Rapid Research Letters* **4,** 13–15; 10.1002/pssr.200903290 (2010).

15. Breitenstein, O., Höffler, H. & Haunschild, J. Photoluminescence image evaluation of solar cells based on implied voltage distribution. *Photovoltaics, Solar Energy Materials, and Technologies: Cancun 2010* **128,** 296–299; 10.1016/j.solmat.2014.05.040 (2014).

16. Haunschild, J., Glatthaar, M., Kasemann, M., Rein, S. & Weber, E. R. Fast series resistance imaging for silicon solar cells using electroluminescence. *Physica Status Solidi RRL* **3,** 227–229; 10.1002/pssr.200903175 (2009).

17. Hoffler, H., Breitenstein, O. & Haunschild, J. Short-Circuit Current Density Imaging Via PL Image Evaluation Based on Implied Voltage Distribution. *IEEE J. Photovolt.* **5,** 613–618; 10.1109/JPHOTOV.2014.2379097 (2015).

18. Mastroianni, S. *et al.* Analysing the effect of crystal size and structure in highly efficient CH3NH3PbI3 perovskite solar cells by spatially resolved photo- and electroluminescence imaging. *Nanoscale* **7,** 19653–19662; 10.1039/C5NR05308K (2015).

19. Hameiri, Z. *et al.* Photoluminescence and electroluminescence imaging of perovskite solar cells. *Progress in Photovoltaics* **23,** 1697–1705; 10.1002/pip.2716 (2015).

20. Okano, M. *et al.* Degradation mechanism of perovskite CH 3 NH 3 PbI 3 diode devices studied by electroluminescence and photoluminescence imaging spectroscopy. *Appl Phys Express* **8,** 102302; 10.7567/APEX.8.102302 (2015).

21. Soufiani, A. M. *et al.* Lessons Learnt from Spatially Resolved Electro- and Photoluminescence Imaging. Interfacial Delamination in CH 3 NH 3 PbI 3 Planar Perovskite Solar Cells upon Illumination. *Advanced Energy Materials* **49,** 1602111; 10.1002/aenm.201602111 (2016).

22. Soufiani, A. M., Kim, J., Ho-Baillie, A., Green, M. & Hameiri, Z. Luminescence Imaging Characterization of Perovskite Solar Cells: A Note on the Analysis and Reporting the Results. *Adv. Energy Mater.* **8,** 1702256; 10.1002/aenm.201702256 (2018).

23. Mundt, L. E. *et al.* Nondestructive Probing of Perovskite Silicon Tandem Solar Cells Using Multiwavelength Photoluminescence Mapping. *IEEE Journal of Photovoltaics* **7,** 1081–1086; 10.1109/JPHOTOV.2017.2688022 (2017).

24. Walter, D. *et al.* On the Use of Luminescence Intensity Images for Quantified Characterization of Perovskite Solar Cells. Spatial Distribution of Series Resistance. *Adv. Energy Mater.* **5,** 1701522; 10.1002/aenm.201701522 (2017).

25. Rietwyk, K. J. *et al.* Light intensity modulated photoluminescence for rapid series resistance mapping of perovskite solar cells. *Nano Energy* **73,** 104755; 10.1016/j.nanoen.2020.104755 (2020).
26. Carstensen, J., Popkirov, G., Bahr, J. & Föll, H. CELLO: an advanced LBIC measurement technique for solar cell local characterization. *Solar Energy Materials and Solar Cells* **76,** 599–611; 10.1016/S0927-0248(02)00270-2 (2003).
27. Würfel, P. & Würfel, U. *Physics of solar sells. From basic principles to advanced concepts.* 3rd ed. (WILEY-VCH, Weinheim, 2016).
28. Calado, P. *et al.* Identifying Dominant Recombination Mechanisms in Perovskite Solar Cells by Measuring the Transient Ideality Factor. *Phys. Rev. Applied* **11**; 10.1103/PhysRevApplied.11.044005 (2019).
29. Kirchartz, T. & Nelson, J. Meaning of reaction orders in polymer:fullerene solar cells. *Phys Rev B* **86**; 10.1103/PhysRevB.86.165201 (2012).
30. Cui, P. *et al.* Planar p–n homojunction perovskite solar cells with efficiency exceeding 21.3%. *Nat. Energy* **4,** 150–159; 10.1038/s41560-018-0324-8 (2019).
31. Edri, E. *et al.* Elucidating the charge carrier separation and working mechanism of CH3NH3PbI3−xClx perovskite solar cells. *Nature communications* **5,** 3461 EP -; 10.1038/ncomms4461 (2014).
32. Cui, P. *et al.* Highly Efficient Electron-Selective Layer Free Perovskite Solar Cells by Constructing Effective p-n Heterojunction. *Sol. RRL* **1,** 1600027; 10.1002/solr.201600027 (2017).
33. Wang, Z. *et al.* High irradiance performance of metal halide perovskites for concentrator photovoltaics. *Nat Energy* **3,** 855–861; 10.1038/s41560-018-0220-2 (2018).
34. Tress, W. *et al.* Interpretation and evolution of open-circuit voltage, recombination, ideality factor and subgap defect states during reversible light-soaking and irreversible degradation of perovskite solar cells. *Energy & Environmental Science* **11,** 151–165; 10.1039/C7EE02415K (2018).
35. Stolterfoht, M. *et al.* Voltage-Dependent Photoluminescence and How It Correlates with the Fill Factor and Open-Circuit Voltage in Perovskite Solar Cells. *ACS Energy Lett.* **4,** 2887–2892; 10.1021/acsenergylett.9b02262 (2019).
36. Geisz, J. F., Steiner, M. A., García, I., Kurtz, S. R. & Friedman, D. J. Enhanced external radiative efficiency for 20.8% efficient single-junction GaInP solar cells. *Appl Phys Lett* **103,** 41118; 10.1063/1.4816837 (2013).
37. Schygulla, P., Heinz, F., Lackner, D. & Dimroth, F. Subcell Development for Wafer-Bonded III-V//Si Tandem Solar Cells. In *2020 47th IEEE Photovoltaic Specialists Conference (PVSC)* (IEEEMonday, June 15, 2020 - Friday, August 21, 2020), pp. 2716–2719.
38. Suckow, S., Pletzer, T. M. & Kurz, H. Fast and reliable calculation of the two-diode model without simplifications. *Progress in Photovoltaics: Research and Applications* **22,** 494–501; 10.1002/pip.2301 (2014).
39. Sinton, R. A. Possibilities for process-control monitoring of electronic material properties during solar-cell manufacture. In *Proceedings 9th Workshop on Crystalline Silicon Solar Cell Materials and Processes,* pp. 67–73.
40. Anaya, M. *et al.* Optical Description of Mesostructured Organic-Inorganic Halide Perovskite Solar Cells. *J. Phys. Chem. Lett.* **6,** 48–53; 10.1021/jz502351s (2015).